

# Searching for cosmological stochastic backgrounds by notching out resolvable compact binary foregrounds with next-generation gravitational-wave detectors

Haowen Zhong <sup>1,\*</sup>, Bei Zhou <sup>2,3,†</sup>, Luca Reali <sup>4,‡</sup>, Emanuele Berti <sup>4,§</sup> and Vuk Mandic <sup>1,¶</sup>

<sup>1</sup>*School of Physics and Astronomy, University of Minnesota, Minneapolis, MN 55455, USA*

<sup>2</sup>*Theoretical Physics Department, Fermi National Accelerator Laboratory, Batavia, Illinois 60510, USA*

<sup>3</sup>*Kavli Institute for Cosmological Physics, University of Chicago, Chicago, Illinois 60637, USA*

<sup>4</sup>*William H. Miller III Department of Physics and Astronomy,  
Johns Hopkins University, Baltimore, Maryland 21218, USA*

(Dated: June 18, 2024)

Stochastic gravitational-wave backgrounds can be of either cosmological or astrophysical origin. The detection of an astrophysical stochastic gravitational-wave background with ground-based interferometers is expected in the near future. Perhaps even more excitingly, the detection of stochastic backgrounds of cosmological origin by future ground-based interferometers could reveal invaluable information about the early Universe. From this perspective, the astrophysical background is a *foreground* that can prevent the extraction of this information from the data. In this paper, we revisit a time-frequency domain notching procedure previously proposed to remove the astrophysical foreground in the context of next-generation ground-based detectors, but we consider the more realistic scenario where we remove individually detectable signals by taking into account the uncertainty in the estimation of their parameters. We find that time-frequency domain masks can still efficiently remove the astrophysical foreground and suppress it to about 5% of its original level. Further removal of the foreground formed by unresolvable events (in particular, unresolvable binary neutron stars), which is about 10 times larger than the residual foreground from realistic notching, would require detector sensitivity improvements. Therefore, the main limitation in the search for a cosmological background is the unresolvable foreground itself, and not the residual of the notching procedure.

## I. INTRODUCTION

As ground-based gravitational-wave (GW) observatories improve in sensitivity, a detection of the astrophysical stochastic gravitational wave background (SGWB) from compact binary coalescence (CBC) events is expected in the near future [1–3]. Besides the SGWB from CBCs, several other interesting SGWBs might be present in the data, e.g. those from supernova explosions [4–8], standard inflation [9–11], axion inflation [12], or cosmic strings [13–16]. Detecting these subdominant SGWBs has significant scientific benefits: the subdominant astrophysical SGWBs potentially contain key information about the properties of their corresponding sources [1, 17, 18], while cosmological SGWBs would open up a unique window to observe the earliest moments of the Universe and to probe physics at energies close to the Planck scale [9–16]. However, the predicted energy densities of these different SGWBs vary by many orders of magnitude, and it is challenging to resolve them with current interferometers unless their amplitude is comparable to, or larger than, the SGWB from CBCs, which in this context is a foreground limiting our ability to observe other SGWBs.

Planned next-generation (XG) ground-based detectors, such as Cosmic Explorer (CE) [19] and the Einstein Telescope (ET) [20], will see an unprecedented increase in sensitivity both to individual CBC events and to stochastic searches, allowing us to probe SGWBs across several orders of magnitude in amplitude [3]. Moreover, they are expected to individually resolve nearly all of the binary black hole (BBH) events and a significant fraction of binary neutron star (BNS) and neutron star-black hole (NSBH) events across the whole Universe [21, 22]. This opens up the possibility of removing the CBC foreground from the data to search for other subdominant SGWBs of both cosmological and astrophysical origin [23, 24].

In practice, however, parameter estimation (PE) uncertainties on the individually resolved signals imply that their subtraction is never perfect, resulting in a residual foreground that is potentially stronger than other targeted SGWB [25–27]. Several techniques have been proposed to reduce this residual foreground, from applying a projection procedure in the time or frequency domain [28, 29] to estimating and subtracting the expected residual power [30, 31]. Alternative techniques that simultaneously fit all the events within a Bayesian framework have also been proposed [32–34], although their computational feasibility in the context of XG detectors has yet to be proven.

In previous work, we proposed a novel notching procedure in the time-frequency domain (different from other approaches that work either in the time or in the frequency domain), where pixels containing CBC signals in time-frequency space are notched out [35]. In that pre-

\* zhong461@umn.edu

† beizhou@fnal.gov

‡ lreali1@jhu.edu

§ berti@jhu.edu

¶ vuk@umn.edu

vious work we assumed that all CBC parameters can be recovered perfectly (i.e., without uncertainty). We computed the resulting sensitivity of the stochastic search after removing all CBC events, and calculated the strength of the SGWB generated by the subthreshold CBC events. Our results showed that this unresolvable CBC foreground was much stronger than the detector noise after foreground cleaning. This suggested that the notching procedure can effectively remove the astrophysical foreground, and that the primary limitation for future cosmological SGWB searches will not be the detector sensitivity, but rather the limit set by the unresolvable CBC foreground.

In this work, we consider a more realistic scenario where only resolvable events can be notched out, and the realistic recovery of CBC parameters is taken into account. We generate BNS and BBH populations consistent with the LIGO-Virgo-KAGRA (LVK) catalog [1]. We adopt a Fisher-matrix approach [36] to estimate the errors on the inferred parameters for resolved events. We then extend our previous procedure to devise a mask for the recovered signals in the time-frequency plane. *We find that even when only resolvable events are removed and the masks used for notching are determined by the recovered CBC parameters, we are still able to remove the foreground from resolved events and suppress the whole foreground generated by all CBC events, including the unresolvable ones, to  $\sim 5.4\%$  of its original level.* The sensitivity to other subdominant SGWBs is thus limited by the foreground from unresolved BNS events, with the residuals from realistic subtraction (of resolved events) providing an additional  $\sim 10\%$  contribution in the remaining foreground after notching.

The rest of the paper is structured as follows. In Sec. II we review the standard process for cross-correlation searches of SGWBs. In Sec. III we provide the details of our CBC population models. In Sec. IV we describe the Fisher-matrix formalism used to estimate the uncertainties associated with CBCs, along with our choices of detector network and waveform model. In Sec. V we discuss our procedure to generate mock data and compute masks for the subsequent notching. In Sec. VI we show the notching results. In Sec. VII we draw our conclusions and outline directions for future work. In Appendix A we discuss the validity of the power-law approximation for the SGWB from CBCs commonly used in the literature.

## II. CROSS-CORRELATION SEARCH FOR THE SGWB

The dimensionless SGWB energy density spectrum is defined by

$$\Omega_{\text{GW}}(f) := \frac{f}{\rho_{c,0}} \frac{d\rho_{\text{GW}}(f)}{df}, \quad (1)$$

where  $d\rho_{\text{GW}}(f)$  is the GW energy density in the frequency bin  $(f, f + df)$ ,  $\rho_{c,0} = 3H_0^2 c^2 / (8\pi G)$  is the

critical energy density to close the Universe,  $c$  is the speed of light,  $G$  is Newton's constant, and  $H_0 = 67.66$  km/s/Mpc [37] is the Hubble constant.

In the SGWB search, we assume a power-law SGWB of the form

$$\Omega_{\text{GW}}(f) = \Omega_\alpha \left( \frac{f}{f_{\text{ref}}} \right)^\alpha, \quad (2)$$

where  $\alpha$  is the power-law index of the GW spectrum, and we choose  $f_{\text{ref}} = 25$  Hz as the reference frequency.

For terrestrial GW detectors, we need to cross-correlate the data from a network consisting of two or more detectors to pick up the common SGWB signal. For a single GW detector, we can write the strain time series as

$$h(t) = F^+ h_+(t) + F^\times h_\times(t), \quad (3)$$

where  $F^{+/\times}$  is the antenna pattern function corresponding to the  $+$  and  $\times$  GW polarization modes, respectively. In a real SGWB search, we usually cut the time strain data into chunks with duration  $T = 60 - 192$  s [2, 3]. However, in our study, we are required to capture the transient features of CBC tracks in the time-frequency domain, which calls for a proper time and frequency resolution. Therefore we choose  $T = 4$  s, as in Ref. [35]. We denote the Fourier transform of these segments by  $\tilde{h}_I(t_i; f_j)$ , where the index ‘‘I’’ refers to the  $I$ th detector in the network,  $t_i$  is the time segment used for the analysis, and  $f_j$  indicates the frequency bin. We define the standard cross-correlation statistics and the corresponding variance estimator for the baseline  $IJ$  as follows [2, 38]:

$$\begin{aligned} \hat{C}_{IJ}(t_i; f_j) &= \left( \frac{20\pi^2 f_j^3}{3H_0^2 T} \right) \frac{\text{Re}[\tilde{h}_I^*(t_i; f_j) \tilde{h}_J(t_i; f_j)]}{\gamma_{IJ}(f_j)} \\ \hat{\sigma}_{IJ}^2(t_i; f_j) &= \left( \frac{20\pi^2 f_j^3}{3H_0^2} \right)^2 \frac{P_{n_I}(t_i; f_j) P_{n_J}(t_i; f_j)}{8T \Delta f \gamma_{IJ}^2(f_j)}. \end{aligned} \quad (4)$$

Here  $\gamma_{IJ}(f_j)$  is the overlap reduction function between the  $I$ th and  $J$ th detectors [38],  $\Delta f = 0.25$  Hz is the Fourier transform resolution, and  $P_{n_I}(t_i; f_j)$  is the power spectral density (PSD) of the  $I$ th detector at time  $t_i$ .

As some of us pointed out in previous work [35], directly estimating the detector noise PSD from the data is particularly challenging, since the presence of the CBC foreground could lead to large biases. Here we assume that the detector noise is perfectly modeled, and we adopt the true PSD used for generating detector noise data to carry out the above calculations.

Having  $\hat{C}_{IJ}(t_i; f_j)$  and  $\hat{\sigma}_{IJ}^2(t_i; f_j)$  at hand, we can combine them to maximize the resulting signal-to-noise ratio:

$$\begin{aligned} \hat{C}_{IJ} &= \frac{\sum_{ij} w(f_j) \hat{C}_{IJ}(t_i; f_j) \hat{\sigma}_{IJ}^{-2}(t_i; f_j)}{\sum_{ij} w^2(f_j) \hat{\sigma}_{IJ}^{-2}(t_i; f_j)}, \\ \hat{\sigma}_{IJ}^{-2} &= \sum_{ij} \frac{w^2(f_j)}{\hat{\sigma}_{IJ}^2(t_i; f_j)}, \end{aligned} \quad (5)$$

with weights defined by  $w(f_j) = \Omega_{\text{GW}}(f_j)/\Omega_\alpha$  [2]. With these definitions,  $\hat{C}_{\text{IJ}}$  is the broadband detection statistic averaged over the entire observation data, normalized so that  $\langle \hat{C}_{\text{IJ}} \rangle = \Omega_\alpha$ . We can perform a weighted average over all time bins of  $\hat{C}_{\text{IJ}}(t_i; f_j)$  and  $\hat{\sigma}_{\text{IJ}}^{-2}(t_i; f_j)$  to get two frequency-domain spectra,  $\hat{C}_{\text{IJ}}(f)$  and  $\hat{\sigma}_{\text{IJ}}^{-2}(f)$ , of the SGWB and detector noise:

$$\begin{aligned}\hat{C}_{\text{IJ}}(f_j) &= \frac{\sum_i \hat{C}_{\text{IJ}}(t_i; f_j) \hat{\sigma}_{\text{IJ}}^{-2}(t_i; f_j)}{\sum_i \hat{\sigma}_{\text{IJ}}^{-2}(t_i; f_j)}, \\ \hat{\sigma}_{\text{IJ}}^{-2}(f_j) &= \sum_i \frac{1}{\hat{\sigma}_{\text{IJ}}^2(t_i; f_j)}.\end{aligned}\quad (6)$$

If we have more than two detectors in the network, we can further combine  $\hat{C}_{\text{IJ}}$  and  $\hat{\sigma}_{\text{IJ}}^{-2}$  among different pairs to obtain

$$\begin{aligned}\hat{C} &= \frac{\sum_{\text{IJ}} \hat{C}_{\text{IJ}} \hat{\sigma}_{\text{IJ}}^{-2}}{\sum_{\text{IJ}} \hat{\sigma}_{\text{IJ}}^{-2}}, \\ \hat{\sigma}^{-2} &= \sum_{\text{IJ}} \frac{1}{\hat{\sigma}_{\text{IJ}}^2},\end{aligned}\quad (7)$$

where IJ denotes the baseline composed by the Ith and Jth detectors, and the summation goes through all possible baselines. Again, we can get spectra  $\hat{C}(f)$  and  $\hat{\sigma}^{-2}(f)$  by a weighted average of  $\hat{C}_{\text{IJ}}(f)$  and  $\hat{\sigma}_{\text{IJ}}^{-2}(f)$ :

$$\begin{aligned}\hat{C}(f) &= \frac{\sum_{\text{IJ}} \hat{C}_{\text{IJ}}(f) \hat{\sigma}_{\text{IJ}}^{-2}(f)}{\sum_{\text{IJ}} \hat{\sigma}_{\text{IJ}}^{-2}(f)}, \\ \hat{\sigma}^{-2}(f) &= \sum_{\text{IJ}} \frac{1}{\hat{\sigma}_{\text{IJ}}^2(f)}.\end{aligned}\quad (8)$$

### III. COMPACT BINARY POPULATIONS

We use the same CBC population models as in Ref. [35], with the mass and redshift distributions described in Secs. III A and III B, respectively. In the simulations, we consider a one-year observation time.

#### A. Mass and angle distributions

For the BBH mass distribution, we employ the `PowerLaw+Peak` model from the latest LVK catalog [1]. For BNS events, we adopt a uniform mass distribution ranging from  $1M_\odot$  to  $2M_\odot$ , in accordance with [1, 39]. We assume the spins to be zero for all binary components, as we expect their impact to be subdominant for our notching procedure. Recent work pointed out that

the inclusion of spin effects could lead to 10 times worse and 20 times worse results for BBHs and BNSs, respectively, when performing subtraction [27]. However, the masks we use for notching are primarily determined by the detector-frame chirp masses, whose inference is not significantly affected by the inclusion of parameters that appear at higher order in the expansion of the phase, such as the spins. For the same reason, we also neglect the effects of nonzero tidal deformability for BNSs. The angular parameters for both BBH and BNS binaries (i.e., inclination angle  $\iota$ , right ascension  $\alpha$ , declination  $\delta$ , and polarization angle  $\psi$ ) are drawn isotropically. We sample the coalescence phase  $\phi_c$  uniformly within  $[0, 2\pi]$ .

#### B. Redshift distribution and merger rate

As in Refs. [25, 26, 35], we draw the redshift  $z$  from a distribution  $p(z)$  such that

$$p(z) = \frac{R_z(z)}{\int_0^{10} R_z(z) dz}, \quad (9)$$

where  $R_z(z)$  is the CBC merger rate per redshift interval over the range  $z \in [0, 10]$  in the detector frame:

$$R_z(z) = \left. \frac{R_m(z) dV}{1+z} \right|_z, \quad (10)$$

$dV/dz$  is the comoving volume element, and  $R_m(z)$  is the merger rate per comoving volume in the source frame:

$$R_m(z) = \int_{t_{\min}}^{t_{\max}} R_f(z_f) P(t_d) dt_d. \quad (11)$$

Here,  $R_f(z_f)$  is the binary formation rate as a function of the redshift at binary formation time  $t_f = t_f(z_f)$ , and  $P(t_d)$  is the distribution of the time delay  $t_d$  between binary formation and merger. For BNSs, we set  $t_{\min} = 20$  Myr, and for BBHs, we set  $t_{\min} = 50$  Myr;  $t_{\max}$  is set to be the Hubble time in both cases. We use a time delay distribution  $p(t_d) \propto 1/t_d$ . We neglect the time needed for two stars to form a binary system and simply model the binary formation rate as following the star formation rate (SFR) [8]:

$$\text{SFR}(z) = \nu \frac{p e^{q(z-z_m)}}{p - q + q e^{p(z-z_m)}}, \quad (12)$$

with  $z_m = 2.00$ ,  $p = 2.37$  and  $q = 1.80$ .

We set the redshift range to  $z \in [0, 10]$ , and we choose the normalization factors  $\nu_{\text{BBH}}$  and  $\nu_{\text{BNS}}$  to be consistent with the inferred LVK merger rates [1]. Specifically, we fix  $\nu_{\text{BBH}}$  so that  $R_{\text{BBH}}(z = 0.2) = 28.1 \text{ Gpc}^{-3} \text{ yr}^{-1}$ , as in Ref. [35]. For BNSs, since performing the analysis for all of the three populations considered in Ref. [35] is computationally expensive, we consider only the MS Model [1], fixing  $R_{\text{BNS}} = 470 \text{ Gpc}^{-3} \text{ yr}^{-1}$ . Both of the rates listed above are well within the uncertainty bands assumed in Refs. [25, 26].

#### IV. ERRORS FROM REALISTIC RECOVERY

We now discuss the Fisher matrix formalism we use to estimate the errors on the inferred CBC parameters, along with technical details on the detector network and waveform models chosen for our analysis.

We consider a network of three XG detectors: two 40-km-long CE located at LIGO Hanford and LIGO Livingston [40, 41], and one ET at the location of Virgo [42]. This extends our previous work, where we focused on CE only [35]. For the CE detectors, we assume the noise PSD corresponding to the second stage of development [43], while for ET, we assume the PSD for the triangular configuration [22]. When we discuss detector networks, we denote the detectors located at Hanford and Livingston as H and L, for brevity. Since one ET is composed of three colocated detectors, we denote them by ET*i* (*i* = 1, 2, 3).

For both BBHs and BNSs, we use the `IMRPhenomXAS` waveform model [44], which is quasi-circular and includes only the dominant mode of the radiation. We neglect Earth-rotation effects, which were found to have a small impact on our results [25, 26]. We set the low-frequency sensitivity limit to be 5 Hz.

In order to assess whether a certain CBC event is detectable, we calculate the matched-filtering signal-to-noise ratio (SNR):

$$\text{SNR} = \sqrt{\langle h(f)|h(f) \rangle}. \quad (13)$$

Here  $\langle \cdot | \cdot \rangle$  is the usual signal inner product,

$$\langle a|b \rangle = 4 \text{Re} \int_0^\infty \frac{\tilde{a}(f)\tilde{b}^*(f)}{P_n(f)} df, \quad (14)$$

where *a* and *b* are two generic signals, and we denote the complex conjugate with an asterisk.

Due to the large size of our catalog, performing a full Bayesian PE for each resolved event is too computationally expensive. Therefore, we estimate the errors within the linear signal approximation [36]. The linear signal approximation is strictly valid only in the high-SNR limit. However, it provides the (Cramer-Rao) lower bound on the variance of the maximum likelihood estimator of the parameters, if it is unbiased [45]. In this sense, our results are likely to provide an optimistic estimate of the parameter errors. We model the posterior probabilities for the parameters of each source as a multivariate normal distribution. The covariance matrix is given by the inverse of the Fisher matrix [36]

$$\Gamma_{\alpha\beta} = \left\langle \frac{\partial h}{\partial \theta^\alpha} \middle| \frac{\partial h}{\partial \theta^\beta} \right\rangle, \quad (15)$$

with  $\theta^\alpha$  denoting the event parameters. As in Refs. [25, 26], we consider a set of 9 parameters:

$$\boldsymbol{\theta} = \left\{ \ln \left( \frac{\mathcal{M}_z}{M_\odot} \right), \eta, \ln \left( \frac{D_L}{\text{Mpc}} \right), \cos \iota, \cos \delta, \alpha, \psi, \phi_c, t_c \right\}. \quad (16)$$

Here,  $\mathcal{M}_c^z = \mathcal{M}_c(1+z)$  is the detector-frame chirp mass, with  $\mathcal{M}_c = (m_1 m_2)^{3/5} / (m_1 + m_2)^{1/5}$ , and  $m_{1,2}$  the component masses;  $D_L$  is the luminosity distance, obtained from the sampled redshift assuming the Planck 2018 cosmology [37]; and  $\eta = (m_1 m_2) / (m_1 + m_2)^2$  is the symmetric mass ratio. Both Eqs. (13), (14) can be naturally extended to a network of  $N_{\text{det}}$  detectors as

$$\begin{aligned} \text{SNR}_{\text{net}} &= \sqrt{\sum_{i=1}^{N_{\text{det}}} \text{SNR}_i}, \\ \Gamma &= \sum_{j=1}^{N_{\text{det}}} \Gamma_j, \end{aligned} \quad (17)$$

where we assume that the noise is uncorrelated among different detectors. To compute the Fisher matrices, we use the public `python` package `GWBENCH` [46].

We neglect the impact of overlapping signals for both detection and PE, estimating the errors on the inferred parameters of each signal independently. For XG detectors, signal confusion has been shown to slightly decrease the detectability of the CBC events at high redshift [47]. The impact on PE is expected to be mild [48–50] unless two or more signals merge within  $\sim 0.5$  s from each other [51–54].

#### V. MOCK DATA GENERATION AND COMPUTATION OF THE MASKS

In this section, we introduce the way we generate mock strain data and how we determine masks to notch out the astrophysical foreground.

We use the `MDC_Generation` package [55, 56] to generate a list of CBC parameters over a one-year long period, based on the population models outlined in Sec. III. We then use `Bilby` [57] to generate time-domain gravitational waveforms with `IMRphenomXAS` and simulate the strain noise series based on the expected noise PSD. We choose the minimum injection frequency to be 5 Hz. The full time strain series consists of the superposition of the pure CBC injections and the noise strain series generated separately in this way.

Compared to our previous work [35], where we assumed that we could recover all CBC parameters perfectly, here we consider a more realistic scenario in which only resolvable signals can be removed and there is a PE uncertainty associated with the recovered CBC parameters.

For BBHs, we use a detection threshold  $\rho_{\text{thr}}^{\text{BBH}} = 8$ . For BNSs, we set  $\rho_{\text{thr}}^{\text{BNS}} = 12$  to reduce the chance of false detections. This is because BNSs, having smaller masses compared to BBHs, generally emit signals with weaker amplitudes during the inspiral phase, making it more challenging to distinguish them from detector noise [23, 25, 26, 58]. For each resolved event, we draw the recovered CBC parameters from a multidimensional

Gaussian distribution  $\mathcal{N}(\hat{\theta}_\alpha, \Gamma_\alpha^{-1})$  with the mean located at the true values of the parameters  $\hat{\theta}_\alpha$ , and  $\Gamma_\alpha$  given by Eq. (17). We use Bilby [57] again to generate the time series based on these recovered parameters.

Throughout this work, we define two types of masks, which we call *ideal masks* and *realistic masks*, respectively. The ideal masks are determined by CBC injections with the true parameters, similarly to Ref. [35], while the realistic masks are instead determined by CBC injections with the recovered parameters. In practice, realistic recovery due to PE uncertainty implies that we can only have access to the realistic masks, but we consider the ideal masks as well for comparison purposes.

To determine the masks, we consider a noise-free time series with resolvable CBC injections only. We use the Python package `pygwb` [59] to perform cross-correlation calculations and obtain  $\hat{C}_{\text{IJ}}(t_i; f_j)$  and  $\hat{\sigma}_{\text{IJ}}(t_i; f_j)$  for a given baseline IJ. From these two quantities, we construct SNR maps as

$$\text{SNR}_{\text{IJ}}(t_i; f_j) = \left| \hat{C}_{\text{IJ}}(t_i; f_j) / \hat{\sigma}_{\text{IJ}}(t_i; f_j) \right|. \quad (18)$$

We introduce an empirical SNR threshold of  $5 \times 10^{-4}$  for identifying CBC tracks, following the methodology detailed in Ref. [35] for selecting an appropriate threshold. We note, however, that in our previous work, the threshold was set on  $\hat{C}_{\text{IJ}}(t_i; f_j)$ , rather than  $\text{SNR}_{\text{IJ}}(t_i; f_j)$ . The motivation for this change is that  $\text{SNR}_{\text{IJ}}(t_i; f_j)$  is more closely related to the SNR for the stochastic search  $\hat{C}_{\text{IJ}}/\hat{\sigma}_{\text{IJ}}$ . While the threshold can, in principle, vary across different baselines and can change over time and frequency, we simplify our approach by applying a uniform threshold across all baselines, time bins, and frequency bins. We emphasize that, even if the time series used for cross correlation in this step are all noise free, we can still estimate  $\hat{\sigma}_{\text{IJ}}(t_i; f_j)$  according to Eq. (4) using the true PSD curves.

We summarize the cross-correlation results of noise-free (CBC only) data in Appendix B (see Tables III and IV). In both cases, the masks are able to remove the resolvable CBC foreground to a level below the detector noise, i.e., with  $\text{SNR} \lesssim 1$ .

## VI. NOTCHING RESULTS

After computing the masks with noise-free data, we now apply them to noise injections to test their performance.

First, we consider the case where we simulate detector noise and all CBC events in our catalog, including the unresolvable ones. For simplicity, we call this scenario the ‘‘Noise+CBC case’’. Then we consider a scenario in which we also simulate a flat ( $\alpha = 0$ ) SGWB with amplitude  $\Omega_\alpha = 4 \times 10^{-11}$  in addition to the Noise+CBC data. We call this the ‘‘Noise+CBC+SGWB case’’. We note that the real cosmological SGWB is not necessarily

flat. Here we choose this specific SGWB only for demonstration purposes. The results of the notching procedure for two scenarios are shown in Table I and Table II, and discussed in Sec. VIA below.

After generating the time series we run `pygwb` to get  $\hat{C}_{\text{IJ}}(t_i; f_j)$  and  $\hat{\sigma}_{\text{IJ}}(t_i; f_j)$ , assuming  $\alpha = 0$  in both cases. We then apply ideal masks and realistic masks upon the time-frequency maps to remove the astrophysical foreground produced by the resolved CBC events. The injection of the SGWB is also done with `pygwb`. Both tables show the results before notching, and after applying ideal masks and realistic masks for all the different baselines. The HL baseline has the highest sensitivity for searches of SGWBs with power-law index  $\alpha = 0$ . This is why the results found by combining all ten baselines are almost identical to the results given by the single HL baseline.

### A. Results of the notching procedure

In the Noise+CBC case (Table I), there are only two remaining components in the data after notching, in addition to detector noise: (i) The CBC foreground from individually unresolved events  $\hat{C}_{\text{unresolvable}}$ , which cannot be further removed; this is effectively the only remaining component present in the ideal mask case [35]; (ii) The residual foreground due to realistic notching  $\hat{C}_{\text{residual}}$ ; this is an additional component which is present when PE uncertainties are taken into account by using realistic masks, due to the residuals from realistic subtraction of resolved signals.

From the last row of Table I we see that the resulting  $\hat{C}$  is reduced from  $3.1 \times 10^{-10}$  to  $1.5 \times 10^{-11}$  after applying the ideal masks, and to  $1.7(1.68) \times 10^{-11}$  after applying the realistic masks. In other words, our notching procedure can still suppress the foreground from all CBC events to  $\sim 5.4\%$  of its original level, even when only resolvable CBC events are removed and the residuals due to realistic subtraction are taken into account. This is one of the main results of this paper.

From the ideal-mask case, we obtain that  $\hat{C}_{\text{unresolvable}} \approx 1.5(1.54) \times 10^{-11}$ , and thus the additional contribution with realistic masks is  $\hat{C}_{\text{residual}} \approx 1.4(1.44) \times 10^{-12}$ . The ratio between the residual foreground and the foreground from unresolvable events is  $\hat{C}_{\text{residual}}/\hat{C}_{\text{unresolvable}} \approx 9.3\%$ . This implies that, despite the additional contribution from realistic removal, the floor for SGWB searches is largely determined by the unresolvable CBC foreground, and not by the residual due to notching. This is consistent with previous conclusions in the idealized case of perfect recovery of the resolved signals [35].

The last row of Table I shows that the combined  $\hat{\sigma}$  is  $1.3 \times 10^{-13}$  before notching, and it increases to  $1.5 \times 10^{-13}$  when we apply either ideal or realistic masks. It is important to note that  $\hat{\sigma}$  increases by 16% after notching, which means that the sensitivity for stochastic searches will be moderately impacted by the foreground cleaning

Baseline	Before notching			Ideal masks applied			Realistic masks applied		
	$\hat{C}_{\text{IJ}}$	$\hat{\sigma}_{\text{IJ}}$	SNR	$\hat{C}_{\text{IJ}}$	$\hat{\sigma}_{\text{IJ}}$	SNR	$\hat{C}_{\text{IJ}}$	$\hat{\sigma}_{\text{IJ}}$	SNR
H-L	$3.2 \times 10^{-10}$	$1.4 \times 10^{-13}$	$2.3 \times 10^3$	$1.5 \times 10^{-11}$	$1.6 \times 10^{-13}$	$9.8 \times 10^1$	$1.6 \times 10^{-11}$	$1.5 \times 10^{-13}$	$1.0 \times 10^2$
H-ET1	$3.1 \times 10^{-10}$	$2.2 \times 10^{-12}$	$1.4 \times 10^2$	$3.2 \times 10^{-11}$	$2.4 \times 10^{-12}$	$1.3 \times 10^1$	$3.4 \times 10^{-11}$	$2.4 \times 10^{-12}$	$1.4 \times 10^1$
H-ET2	$2.2 \times 10^{-10}$	$1.2 \times 10^{-12}$	$1.8 \times 10^2$	$9.0 \times 10^{-12}$	$1.8 \times 10^{-12}$	5.0	$1.6 \times 10^{-11}$	$1.8 \times 10^{-12}$	8.9
H-ET3	$2.7 \times 10^{-10}$	$1.3 \times 10^{-12}$	$2.1 \times 10^2$	$1.5 \times 10^{-11}$	$1.7 \times 10^{-12}$	8.8	$1.9 \times 10^{-11}$	$1.7 \times 10^{-12}$	$1.1 \times 10^1$
L-ET1	$2.3 \times 10^{-10}$	$1.5 \times 10^{-12}$	$1.5 \times 10^2$	$1.3 \times 10^{-11}$	$2.3 \times 10^{-12}$	5.7	$2.0 \times 10^{-11}$	$2.3 \times 10^{-12}$	8.9
L-ET2	$2.5 \times 10^{-10}$	$1.0 \times 10^{-12}$	$2.5 \times 10^2$	$1.1 \times 10^{-11}$	$1.3 \times 10^{-12}$	7.9	$1.5 \times 10^{-11}$	$1.3 \times 10^{-12}$	$1.2 \times 10^1$
L-ET3	$3.8 \times 10^{-10}$	$2.2 \times 10^{-12}$	$1.7 \times 10^2$	$1.8 \times 10^{-11}$	$2.4 \times 10^{-12}$	7.5	$2.0 \times 10^{-11}$	$2.4 \times 10^{-12}$	8.2
ET1-ET2	$3.1 \times 10^{-10}$	$1.0 \times 10^{-12}$	$3.0 \times 10^2$	$2.5 \times 10^{-11}$	$1.7 \times 10^{-12}$	$1.5 \times 10^1$	$4.1 \times 10^{-11}$	$1.7 \times 10^{-12}$	$2.5 \times 10^1$
ET1-ET3	$3.2 \times 10^{-10}$	$1.1 \times 10^{-12}$	$3.0 \times 10^2$	$2.9 \times 10^{-11}$	$1.7 \times 10^{-12}$	$1.7 \times 10^1$	$4.5 \times 10^{-11}$	$1.7 \times 10^{-12}$	$2.7 \times 10^1$
ET2-ET3	$3.2 \times 10^{-10}$	$1.1 \times 10^{-12}$	$3.0 \times 10^2$	$2.8 \times 10^{-11}$	$1.8 \times 10^{-12}$	$1.6 \times 10^1$	$4.4 \times 10^{-11}$	$1.7 \times 10^{-12}$	$2.5 \times 10^1$
Combined	$3.1 \times 10^{-10}$	$1.3 \times 10^{-13}$	$2.4 \times 10^3$	$1.5 \times 10^{-11}$	$1.5 \times 10^{-13}$	$1.0 \times 10^2$	$1.7 \times 10^{-11}$	$1.5 \times 10^{-13}$	$1.1 \times 10^2$

TABLE I. Notching results for the Noise+CBC case. The power law index  $\alpha$  is set to  $\alpha = 0$ . The CBC injections include all events, including the unresolvable ones. Columns 2, 3 and 4 list  $\hat{C}_{\text{IJ}}$ ,  $\hat{\sigma}_{\text{IJ}}$  and  $\text{SNR} = \hat{C}_{\text{IJ}}/\hat{\sigma}_{\text{IJ}}$  before notching. Columns 5, 6, and 7 are the results after applying ideal masks, which are determined by the true CBC parameters. Columns 8, 9, and 10 list the results after applying realistic masks, calculated using the resampled CBC parameters.

Baseline	Before notching			Ideal masks applied			Realistic masks applied		
	$\hat{C}_{\text{IJ}}$	$\hat{\sigma}_{\text{IJ}}$	SNR	$\hat{C}_{\text{IJ}}$	$\hat{\sigma}_{\text{IJ}}$	SNR	$\hat{C}_{\text{IJ}}$	$\hat{\sigma}_{\text{IJ}}$	SNR
H-L	$3.6 \times 10^{-10}$	$1.4 \times 10^{-13}$	$2.6 \times 10^3$	$5.5 \times 10^{-11}$	$1.6 \times 10^{-13}$	$3.5 \times 10^2$	$5.6 \times 10^{-11}$	$1.5 \times 10^{-13}$	$3.6 \times 10^2$
H-ET1	$3.5 \times 10^{-10}$	$2.2 \times 10^{-12}$	$1.6 \times 10^2$	$7.1 \times 10^{-11}$	$2.4 \times 10^{-12}$	$2.9 \times 10^1$	$7.4 \times 10^{-11}$	$2.4 \times 10^{-12}$	$3.1 \times 10^1$
H-ET2	$2.6 \times 10^{-10}$	$1.2 \times 10^{-12}$	$2.1 \times 10^2$	$4.9 \times 10^{-12}$	$1.8 \times 10^{-12}$	$2.7 \times 10^1$	$5.6 \times 10^{-11}$	$1.8 \times 10^{-12}$	$3.1 \times 10^1$
H-ET3	$3.1 \times 10^{-10}$	$1.3 \times 10^{-12}$	$2.4 \times 10^2$	$5.5 \times 10^{-11}$	$1.7 \times 10^{-12}$	$3.2 \times 10^1$	$5.8 \times 10^{-11}$	$1.7 \times 10^{-12}$	$3.5 \times 10^1$
L-ET1	$2.7 \times 10^{-10}$	$1.5 \times 10^{-12}$	$1.8 \times 10^2$	$5.3 \times 10^{-11}$	$2.3 \times 10^{-12}$	$2.3 \times 10^1$	$6.0 \times 10^{-11}$	$2.3 \times 10^{-12}$	$2.6 \times 10^1$
L-ET2	$2.9 \times 10^{-10}$	$1.0 \times 10^{-12}$	$2.9 \times 10^2$	$5.1 \times 10^{-11}$	$1.3 \times 10^{-12}$	$3.8 \times 10^1$	$5.5 \times 10^{-11}$	$1.3 \times 10^{-12}$	$4.2 \times 10^1$
L-ET3	$4.2 \times 10^{-10}$	$2.2 \times 10^{-12}$	$1.9 \times 10^2$	$5.8 \times 10^{-11}$	$2.4 \times 10^{-12}$	$2.4 \times 10^1$	$6.0 \times 10^{-11}$	$2.4 \times 10^{-12}$	$2.5 \times 10^1$
ET1-ET2	$3.4 \times 10^{-10}$	$1.0 \times 10^{-12}$	$3.3 \times 10^2$	$6.5 \times 10^{-11}$	$1.7 \times 10^{-12}$	$3.8 \times 10^1$	$8.1 \times 10^{-11}$	$1.7 \times 10^{-12}$	$4.9 \times 10^1$
ET1-ET3	$3.6 \times 10^{-10}$	$1.1 \times 10^{-12}$	$3.4 \times 10^2$	$6.9 \times 10^{-11}$	$1.7 \times 10^{-12}$	$3.9 \times 10^1$	$8.5 \times 10^{-11}$	$1.7 \times 10^{-12}$	$5.0 \times 10^1$
ET2-ET3	$3.6 \times 10^{-10}$	$1.1 \times 10^{-12}$	$3.4 \times 10^2$	$6.7 \times 10^{-11}$	$1.8 \times 10^{-12}$	$3.8 \times 10^1$	$8.3 \times 10^{-11}$	$1.7 \times 10^{-12}$	$4.8 \times 10^1$
Combined	$3.5 \times 10^{-10}$	$1.3 \times 10^{-13}$	$2.8 \times 10^3$	$5.5 \times 10^{-11}$	$1.5 \times 10^{-13}$	$3.7 \times 10^2$	$5.7 \times 10^{-11}$	$1.5 \times 10^{-13}$	$3.8 \times 10^2$

TABLE II. Same as Table I, but for the Noise+CBC+SGWB case.

procedure. This is also consistent with the conclusions drawn in Ref. [35].

Table I lists the values of  $\hat{C}_{\text{IJ}}$  and  $\hat{\sigma}_{\text{IJ}}$  combined across all frequency bins. In Fig. 1 we also show  $\hat{C}(f)$  and  $\hat{\sigma}(f)$  as functions of frequency, when we combine all ten baselines. The red, blue<sup>1</sup> and orange curves show  $\hat{C}(f)$  before applying masks, after applying realistic masks, and after applying ideal masks, respectively. We estimate the residual from realistic subtraction  $\hat{C}_{\text{residual}}$  (shown in green) by taking the difference between the blue and orange curves. The combined sensitivity  $\hat{\sigma}(f)$  in the three cases (before notching, ideal masks, and realistic masks) are overplotted in gray with different line styles (solid, dashed, and dot-dashed, respectively).

<sup>1</sup> The turning point of the red and blue curves around  $\sim 6$  Hz turns out to be a numerical artifact. When injecting CBC signals into the time series, we need to set a minimum frequency, which we choose to be  $f_{\text{min}} = 5$  Hz. Also we note that when applying cross-correlation using `pygwb`, a cutoff frequency needs to be specified. We also set  $f_{\text{cut}} = 5$  Hz in the analysis. Had we set lower minimum and cutoff frequency the turning point in  $\hat{C}(f)$  around 6 Hz would not be present. However, setting a lower minimum frequency would result in much longer computational times. We note that the most sensitive frequency range for SGWB searches is around  $\mathcal{O}(10)$  Hz, so the impact of the chosen frequency cutoff on the resulting  $\hat{C}$  is minimal.

The curves for ideal and realistic masks are in remarkable agreement within the frequency range  $f \sim 10 - 50$  Hz, which coincides with the most sensitive band of the stochastic search for  $\alpha = 0$ . This illustrates the capability of realistic masks to remove resolvable CBC signals with high accuracy. The residual foreground is relatively loud in the low-frequency range  $f \sim 5 - 10$  Hz, because CBC signals overlap significantly in this range [50]. Comparing to Fig. 2 of Ref. [35], we notice that nearly all the pixels at those low frequencies are notched out. Therefore, a slight bias in the masks coming from PE uncertainties would result in a relatively loud residual.

We highlight that in the frequency range  $f \gtrsim 10$  Hz, the green curve (residual foreground) is well below the gray curves (detector noise). This implies that the residual foreground due to realistic notching has minimal impact on the search for the cosmological SGWB. Furthermore, we emphasize that neither the gray curves nor the green curve limit the search for the cosmological SGWB. *The real limit on the detectability of the cosmological SGWB is set by the blue curve*, which represents the superposition of the unresolvable foreground and of the residual foreground. As we discussed, the unresolvable foreground is about ten times stronger than the residual foreground. This confirms that the unresolvable CBC foreground is the main obstacle in the search for the cosmological SGWB. In Table II and in the right panel

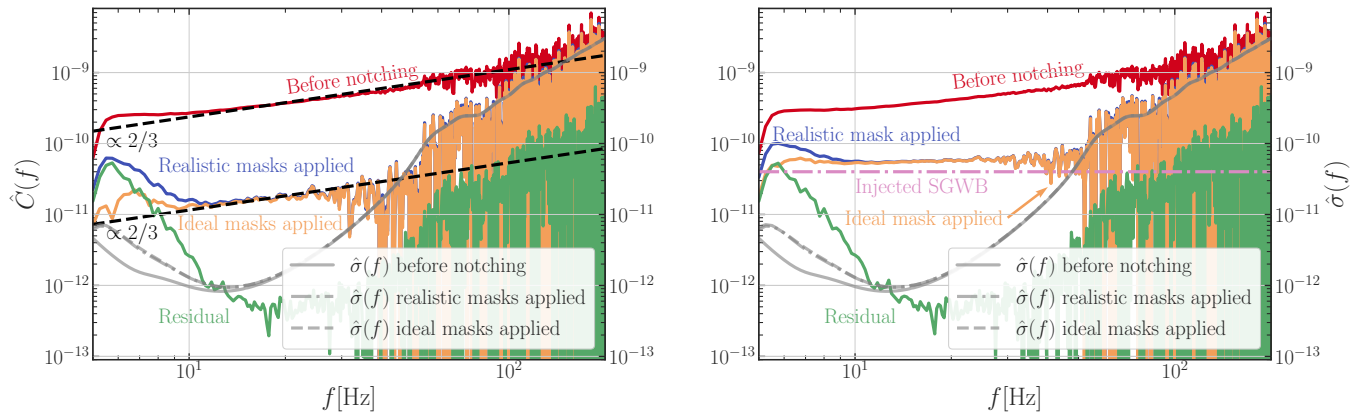


FIG. 1. Left panel: combined  $\hat{C}(f)$  and  $\hat{\sigma}(f)$  for the Noise+CBC case. Right panel: same, but for the Noise+CBC+SGWB case (the injected SGWB is shown by the dot-dashed pink curve). The red, orange, and blue curves correspond to the results before notching, after applying ideal masks, and after applying realistic masks, respectively. The curve labeled as “residual” (in green) is the difference between the blue and orange curves. The combined sensitivity  $\hat{\sigma}(f)$  is plotted in gray: the solid, dashed, and dot-dashed gray curves correspond to the sensitivity before notching, after applying ideal masks, and after applying realistic masks, respectively.

of Fig. 1, we show the same results as Table I and the left panel of Fig. 1, but with an additional flat ( $\alpha = 0$ ) stochastic background with  $\Omega_{\text{ref}} = 4 \times 10^{-11}$  injected into the data. As mentioned above, the astrophysical foreground is suppressed by an order of magnitude, but the strength of the remaining astrophysical foreground is comparable to the injected cosmological SGWB. Therefore, even though the SNR is as large as  $3.8 \times 10^2$ , we still cannot claim a convincing detection of the cosmological SGWB. Better methods will be required to separate the remaining astrophysical foreground from the cosmological background of interest. This is an interesting topic for future work.

### B. Percentage of bins removed and missing rate

We now assess in more detail the performance of the realistic masks relative to the ideal masks.

In Fig. 2 we show the percentage of bins removed as a function of frequency. The red curve is exactly the same as the orange curve in Fig. 2 of Ref. [35], where we assumed we could detect all CBC events (including the unresolvable ones) and recover CBC parameters perfectly. The yellow and blue curves correspond to the results after applying realistic masks and ideal masks, respectively. The gray curve shows the sensitivity  $\hat{\sigma}(f)$  before notching. The difference in starting frequencies between the red curve and the other two stems from the different choices of  $f_{\text{min}}$  in the two analyses. As remarked in Ref. [35], the three peaks in the red curve can be attributed to the zeros in the overlap reduction function  $\gamma_{\text{IJ}}$  that are specific to the HL baseline. Transitioning to an SNR-based threshold and incorporating a wider array of baselines transforms these peaks into dips, with a corresponding shift in their locations.

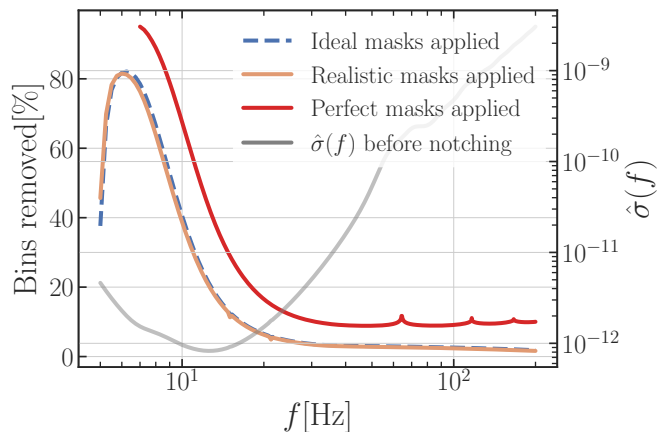


FIG. 2. Percentage of bins removed as a function of frequency. The red curve is the orange curve in Fig. 2 of Ref. [35], which characterizes the proportion of frequencies bins removed by the *perfect masks*, which remove all CBC events including unresolvable ones. The orange curve and blue dashed curve correspond to the results of the realistic masks and ideal masks, respectively. The two curves coincide quite well. For reference, the combined sensitivity  $\hat{\sigma}(f)$  before notching is plotted in gray.

The yellow and blue curves nearly overlap with each other. This confirms once again the similar performance of realistic masks and ideal masks discussed above. The qualitative behavior of the three curves as a function of frequency is similar, but the orange and blue curves are both well below the red curve in the whole frequency band. This is because in this work, we distinguish between resolvable and unresolvable signals, and the pixels containing the latter component survive even after the notching procedure.

For a specific frequency, we can define a “missing rate”

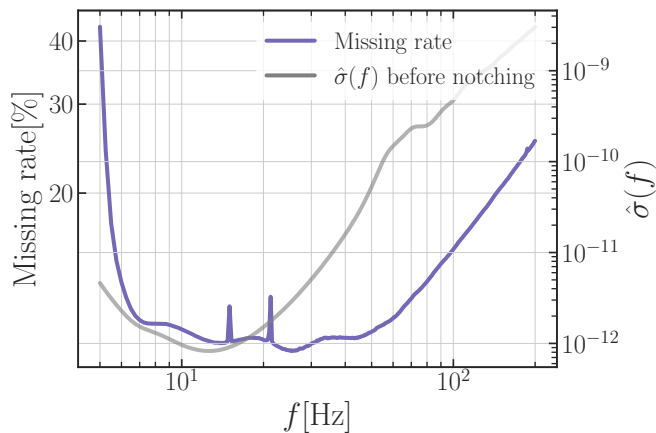


FIG. 3. Missing rate as a function of frequency. The missing rate is defined as the average percentage of pixels that are removed by the ideal masks yet kept by the realistic masks, relative to the total number of pixels removed by the ideal masks. For reference, the combined sensitivity  $\hat{\sigma}(f)$  before notching is plotted in gray.

as the average percentage of pixels that are removed by the ideal masks yet kept by the realistic masks,  $\Delta N(f)$ , normalized to the total number of pixels removed by the ideal masks,  $\hat{N}(f)$ :

$$\text{Missing Rate}(f) = \left\langle \frac{\Delta N(f)}{\hat{N}(f)} \right\rangle_{\text{masks}}. \quad (19)$$

In Fig. 3 we plot the missing rate as a function of frequency. For reference, we also plot the combined sensitivity  $\hat{\sigma}(f)$  before notching. The missing rate is relatively high at low and high frequencies, while it reaches a minimum value in the frequency range  $f \sim 10\text{--}100$  Hz, where our search is most sensitive, and therefore the shape of CBC tracks in the time-frequency domain is best determined. Since we miss the fewest pixels in our most sensitive band, the resulting  $\hat{C}$  after applying realistic masks should be rather close to  $\hat{C}$  after applying ideal masks in this frequency band. These findings are consistent with those in Table I, Table II and Fig. 1.

### C. Physical interpretation

From the above discussion, it is clear that the notching procedure is still effective at suppressing the foreground from resolved signals even when PE uncertainties are taken into account. These findings are significantly more optimistic than previous work by some of us [25, 26], which estimated the residual foreground from realistic subtraction in the frequency domain to be comparable to the original foreground.

To understand the reason for this improvement, it is useful to think about which binary parameters are mainly responsible for realistic subtraction in the two different

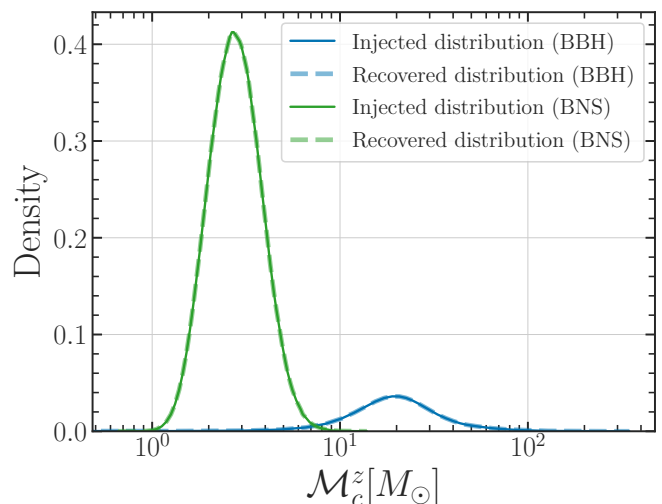


FIG. 4. Injected and recovered distribution of detector-frame chirp masses,  $\mathcal{M}_c^z$ , for BBH and BNS systems. The recovered distribution coincides with the injected distribution quite well.

approaches. In the analysis of Ref. [25, 26], the residuals are dominated by the errors in luminosity distance and coalescence phase (which, in turn, is strongly correlated with other extrinsic parameters, such as the polarization angle). These parameters are poorly constrained for a significant fraction of events even with a network of XG detectors. By contrast, the performance of a mask in the notching procedure is largely determined by how well we can recover the location of the time-frequency track for each event. At leading (quadrupolar) order, the time-frequency evolution for a CBC in the inspiral phase is set by [60]

$$f(t, t_c; \mathcal{M}_c^z) = \frac{1}{\pi} \left( \frac{5}{256(t_c - t)} \right)^{\frac{3}{8}} \left( \frac{G\mathcal{M}_c^z}{c^3} \right)^{-\frac{5}{8}}. \quad (20)$$

Given that most events in XG detectors are inspiral-dominated, this approximation works well for the vast majority of our catalogs. Hence, the location of a CBC track in the time-frequency plane is mostly determined by the detector-frame chirp mass  $\mathcal{M}_c^z$ . Given an accurate recovery of  $\mathcal{M}_c^z$ , the masks computed according to biased injections can still be effective at removing astrophysical foregrounds.

To confirm this interpretation, in Fig. 4, we compare the injected and recovered distributions of detector-frame chirp masses for our BBH and BNS catalogs, respectively. The two histograms show remarkable agreement for both BBHs and BNSs, because the chirp mass is constrained extremely well with XG observatories [61–63]. This precision guarantees that even if the amplitude of individual events is recovered poorly, we can still accurately determine the CBC chirps in the time-frequency domain, such that the notching procedure is effective.

## VII. DISCUSSION AND CONCLUSIONS

In this work, we improve the notching method of Ref. [35] by extending it to a more realistic scenario where not all CBC signals are resolved and where PE uncertainties on the resolved signals are taken into account. We generate BBH and BNS catalogs consistent with the observed LVK populations, and for each resolved event, we estimate the errors on the inferred parameters with a Fisher matrix approach. We compute realistic masks on the recovered CBC signals by resampling their parameters while taking into account the corresponding uncertainties. We apply these realistic masks to notch out the resolved signals in the time-frequency domain. We then compare the result of cross-correlation SGWB searches after this notching procedure with the previous case, where ideal masks were computed by using the true parameters of the injected signals.

We find that the realistic masks perform remarkably well. Consistent with the results of Ref. [25, 26], the amplitude of the foreground in the frequency domain from the resampled parameters can be significantly biased. The poor recovery of luminosity distance, along with the fact that close-by events dominate the foreground, leads to a CBC foreground before notching that is significantly larger when PE errors are taken into account (see Tables III and IV). However, the tracks in the time-frequency plane are mainly determined by the detector-frame chirp mass  $\mathcal{M}_c^z$ , which is constrained to high precision for most events, thus the notching procedure is still very effective at suppressing the CBC foreground.

Assuming a flat ( $\alpha = 0$ ) power-law search, we find that the residual CBC foreground  $\hat{C}$  due to realistic notching is  $\sim 10\%$  of the foreground from unresolved signals that cannot be removed. With our assumptions on the BBH and BNS merger rate, we find that the total foreground is reduced to about  $\sim 5.4\%$  of its original value.

It is important to point out some caveats about the notching procedure used here, and some directions in which it could be further improved. We only resample CBC parameters once for each resolvable event, but multiple draws could be made for low-SNR events to better remove their tracks in the time-frequency plane. However, this also means notching out more pixels, which reduces the detectability of a subdominant SGWB. A more detailed study is needed to understand whether multiple draws would be effective. We assume that the detector noise is perfectly known, while in practice estimating the detector PSD in the presence of glitches, non-stationary noise, and the foreground from unresolved CBC events can be challenging. We neglect the impact of waveform systematics, which is subdominant compared to current astrophysical uncertainties, but still relevant for correctly estimating the foreground [25, 26]. Finally, we neglect astrophysical uncertainties in the CBC catalogs. In particular, we only consider one possible value of the BNS merger rate, which is within the large uncertainty of cur-

rent LVK catalogs. If the number of unresolved events is larger, either due to higher merger rates overall or larger contributions at higher redshifts (e.g. [64, 65]), the CBC foreground after notching may be significantly higher. However, this would not affect the main conclusion of this work – i.e., that including uncertainties in the binary parameters does not significantly affect the notching method. Finally, we neglect the contribution of NSBH binaries, which can produce an unresolved foreground comparable to the one from BNSs in XG detectors [66]. All of these limitations should be addressed in future work.

Overall, our results are consistent with Ref. [35], which suggests that the limiting factor in the sensitivity of XG detectors to stochastic searches will be the CBC foreground from individually unresolved signals, which cannot be further notched out. It is important to develop techniques to separate different SGWB components from the unresolved CBC foreground after notching, which in turn requires accurate modeling of the CBC foreground from unresolved events.

Several techniques to address this issue can and should be explored in the future. For instance, template-based methods that simultaneously fit for both resolved and unresolved signals within a Bayesian framework have been proposed [32–34]. However, the work of Ref. [67] suggests that care should be taken when using these methods, as they may be probing significantly lower redshifts compared to the standard cross-correlation searches. Techniques that leverage principal-component analysis [68] or neural ratio estimation [69] have been proposed in the context of LISA, and they could find application also in the context of XG detectors.

## ACKNOWLEDGMENTS

We thank Arianna Renzini for providing useful comments and suggestions on a first draft of this manuscript. The authors are grateful for computational resources provided by the LIGO Laboratory and supported by National Science Foundation (NSF) Grants PHY-0757058 and PHY-0823459. E. Berti and L. Reali are supported by NSF Grants No. AST-2307146, PHY-2207502, PHY-090003 and PHY-20043, by NASA Grants No. 20-LPS20-0011 and 21-ATP21-0010, by the John Templeton Foundation Grant 62840, by the Simons Foundation, and by the Italian Ministry of Foreign Affairs and International Cooperation grant No. PGR01167. B. Zhou is supported by Fermilab, which is managed by the Fermi Research Alliance, LLC, acting under Contract No. DE-AC02-07CH11359. H. Zhong and V. Mandic were in part supported by the NSF grants PHY-2110238 and NRT-1922512. This work was carried out at the Advanced Research Computing at Hopkins (ARCH) core facility ([rockfish.jhu.edu](http://rockfish.jhu.edu)), which is supported by the NSF Grant No. OAC-1920103. The authors acknowledge the Texas Advanced Computing Center (TACC) at The University of Texas at Austin for providing HPC, visualiza-

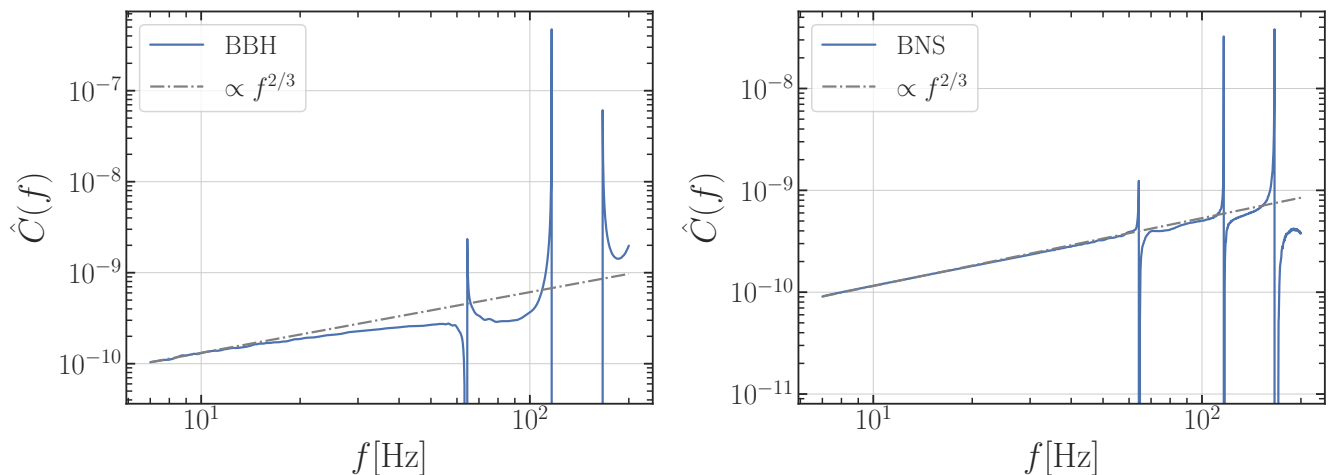


FIG. 5.  $\hat{C}(f)$  for BBH and BNS systems. The gray dotted-dashed lines are included for comparison and represent the  $f^{2/3}$  power-law, showcasing the typical gravitational wave frequency evolution characteristic of compact binary inspirals. The spectral behavior of  $\hat{C}(f)$  for BBH systems exhibits a notable deviation from the  $f^{2/3}$  power-law at frequencies greater than 20 Hz. In contrast, for BNS systems,  $\hat{C}(f)$  aligns closely with the  $f^{2/3}$  power-law across the entire frequency band of interest. The peaks in the curves are due to zero points in the overlap reduction function (see. Eq. (4)).

tion, database, or grid resources that have contributed to the research results reported within this paper [70]. URL: <http://www.tacc.utexas.edu>.

### Appendix A: Validity of the power-law approximation

In Fig. 1, the attentive reader might have noticed that the foreground before notching shows a deviation from the  $f^{2/3}$  power law expected for SGWBs from inspiral-dominated CBCs [2, 16]. This power-law approximation stems from the fact that, at leading order, the GW amplitude for a signal in the inspiral phase scales as  $A(f) \sim f^{-7/6}$  [60, 71]. Given that the cross-correlation  $C(f)$  (or equivalently the energy density  $\Omega_{\text{GW}}$ ) is proportional to  $C(f) \sim f^3 |A(f)|^2$  (see Eq. (4)), an isotropic SGWB generated by the superposition of inspiralling CBCs should scale as  $C(f) \sim \Omega_{\text{GW}}(f) \sim f^{2/3}$ .

However, waveform models such as the IMRPhenomXAS model considered here include higher-order corrections to the inspiral [44], which introduce additional power-law scalings to the expansion for the amplitude, and thus a deviation from the  $f^{2/3}$  scaling. These corrections become more important close to merger and for high-mass systems. This expectation can be confirmed by injecting BBH and BNS events separately into two sets of time series, and computing  $\hat{C}(f)$  for both sets. We show the results in Fig. 5, where the left panel corresponds to BBHs and the right panel to BNSs. In both cases, we overplot the  $\sim f^{2/3}$  scaling for comparison. For BBHs there is an obvious deviation from the  $f^{2/3}$  scaling at frequencies  $f \gtrsim 20$  Hz, while we recover the standard behavior at lower frequencies. On the contrary,  $\hat{C}(f)$  for BNSs is in good agreement with the  $f^{2/3}$  power-law across the entire

frequency band of interest. These results are consistent with the expectation that corrections to the leading-order scaling of the amplitude are relevant for massive systems in the later phases of their inspiral.

The  $f^{2/3}$  approximation is widely used in the literature (see e.g. [2]), and it should be taken with care. Using this scaling, or even approximating the CBC foreground with a single power law, may not always be a good assumption for ground-based detectors, particularly within the frequency range of current interferometers ( $f \gtrsim 20 - 25$  Hz). For BBHs, these scalings should be tested in greater detail using different waveform models. We leave these studies to future work.

### Appendix B: Notching results for noise-free frames

Table III shows the results for the idealized case where we inject the resolvable CBC events with their true parameters. Each row details the results for a certain baseline, with the last row showing the results combining all of the ten baselines. The second to fourth columns represent the values of  $\hat{C}_{\text{IJ}}$ ,  $\hat{\sigma}_{\text{IJ}}$  and SNR before applying any masks. The subsequent columns, from fifth to seventh, represent the results after applying the ideal masks. Table IV is similar, but we now inject resolvable CBC events with resampled parameters.

From the second and fifth columns of Tables III and IV we observe that the values of  $\hat{C}_{\text{IJ}}$  for different baselines before notching are different even when we take  $\hat{\sigma}_{\text{IJ}}$  into account. This is because the expected power-law index  $\alpha$  for the SGWB generated by an astrophysical foreground should be close to  $2/3$  (possibly with some deviations, as discussed in Appendix A) while here for simplicity we use  $\alpha = 0$ , i.e., we assume the cosmological background

Baseline	Before notching			Ideal masks applied		
	$\hat{C}_{IJ}$	$\hat{\sigma}_{IJ}$	SNR	$\hat{C}_{IJ}$	$\hat{\sigma}_{IJ}$	SNR
H-L	$3.0 \times 10^{-10}$	$1.4 \times 10^{-13}$	$2.2 \times 10^3$	$6.7 \times 10^{-14}$	$1.6 \times 10^{-13}$	$4.3 \times 10^{-1}$
H-ET1	$2.8 \times 10^{-10}$	$2.2 \times 10^{-12}$	$1.3 \times 10^2$	$1.4 \times 10^{-13}$	$2.4 \times 10^{-12}$	$5.6 \times 10^{-2}$
H-ET2	$2.1 \times 10^{-10}$	$1.2 \times 10^{-12}$	$1.8 \times 10^2$	$3.0 \times 10^{-13}$	$1.8 \times 10^{-12}$	$1.6 \times 10^{-1}$
H-ET3	$2.5 \times 10^{-10}$	$1.3 \times 10^{-12}$	$2.0 \times 10^2$	$1.7 \times 10^{-13}$	$1.7 \times 10^{-12}$	$1.0 \times 10^{-1}$
L-ET1	$2.2 \times 10^{-10}$	$1.5 \times 10^{-12}$	$1.4 \times 10^2$	$3.1 \times 10^{-13}$	$2.3 \times 10^{-12}$	$1.3 \times 10^{-1}$
L-ET2	$2.5 \times 10^{-10}$	$1.0 \times 10^{-12}$	$2.4 \times 10^2$	$2.3 \times 10^{-13}$	$1.3 \times 10^{-12}$	$1.8 \times 10^{-1}$
L-ET3	$3.7 \times 10^{-10}$	$2.2 \times 10^{-12}$	$1.6 \times 10^2$	$1.6 \times 10^{-13}$	$2.4 \times 10^{-12}$	$6.7 \times 10^{-1}$
ET1-ET2	$2.8 \times 10^{-10}$	$1.0 \times 10^{-12}$	$2.7 \times 10^2$	$7.7 \times 10^{-13}$	$1.7 \times 10^{-12}$	$4.5 \times 10^{-1}$
ET1-ET3	$2.9 \times 10^{-10}$	$1.1 \times 10^{-12}$	$2.7 \times 10^2$	$7.9 \times 10^{-13}$	$1.7 \times 10^{-12}$	$4.5 \times 10^{-1}$
ET2-ET3	$3.0 \times 10^{-10}$	$1.1 \times 10^{-12}$	$2.8 \times 10^2$	$8.2 \times 10^{-13}$	$1.8 \times 10^{-12}$	$4.6 \times 10^{-1}$
Combined	$3.0 \times 10^{-10}$	$1.3 \times 10^{-13}$	$2.3 \times 10^3$	$8.9 \times 10^{-14}$	$1.5 \times 10^{-13}$	$5.9 \times 10^{-1}$

TABLE III. Notching results for the noise-free case, where the data for cross-correlation only contains the resolvable CBC events. The power law index  $\alpha$  is set to  $\alpha = 0$ . The first column lists baselines we consider in the analysis: H for Hanford, L for Livingston, and ET*i* ( $i = 1, 2, 3$ ) for the  $i$ th ET detector. The second, third, and fourth columns list  $\hat{C}_{IJ}$ ,  $\hat{\sigma}_{IJ}$ , and  $\text{SNR} = \hat{C}_{IJ}/\hat{\sigma}_{IJ}$  before notching. The fifth, sixth, and seventh columns are the results after applying ideal masks, which are determined by the true CBC parameters.

Baseline	Before notching			Realistic masks applied		
	$\hat{C}_{IJ}$	$\hat{\sigma}_{IJ}$	SNR	$\hat{C}_{IJ}$	$\hat{\sigma}_{IJ}$	SNR
H-L	$8.0 \times 10^{-10}$	$1.4 \times 10^{-13}$	$5.9 \times 10^3$	$7.0 \times 10^{-14}$	$1.5 \times 10^{-13}$	$4.5 \times 10^{-1}$
H-ET1	$1.4 \times 10^{-10}$	$2.2 \times 10^{-12}$	$6.5 \times 10^1$	$1.4 \times 10^{-13}$	$2.4 \times 10^{-12}$	$5.9 \times 10^{-2}$
H-ET2	$8.5 \times 10^{-10}$	$1.2 \times 10^{-12}$	$7.2 \times 10^2$	$3.3 \times 10^{-13}$	$1.8 \times 10^{-12}$	$1.9 \times 10^{-1}$
H-ET3	$9.6 \times 10^{-10}$	$1.3 \times 10^{-12}$	$7.6 \times 10^2$	$2.0 \times 10^{-13}$	$1.7 \times 10^{-12}$	$1.2 \times 10^{-1}$
L-ET1	$7.1 \times 10^{-10}$	$1.5 \times 10^{-12}$	$4.7 \times 10^2$	$3.3 \times 10^{-13}$	$2.3 \times 10^{-12}$	$1.5 \times 10^{-1}$
L-ET2	$1.0 \times 10^{-9}$	$1.0 \times 10^{-12}$	$1.0 \times 10^3$	$2.6 \times 10^{-13}$	$1.3 \times 10^{-12}$	$2.0 \times 10^{-1}$
L-ET3	$8.4 \times 10^{-10}$	$2.2 \times 10^{-12}$	$3.8 \times 10^2$	$1.7 \times 10^{-13}$	$2.4 \times 10^{-12}$	$7.0 \times 10^{-2}$
ET1-ET2	$7.4 \times 10^{-10}$	$1.0 \times 10^{-12}$	$7.2 \times 10^2$	$8.3 \times 10^{-13}$	$1.7 \times 10^{-12}$	$5.0 \times 10^{-1}$
ET1-ET3	$7.7 \times 10^{-10}$	$1.1 \times 10^{-12}$	$7.2 \times 10^2$	$8.2 \times 10^{-13}$	$1.7 \times 10^{-12}$	$4.8 \times 10^{-1}$
ET2-ET3	$7.9 \times 10^{-10}$	$1.1 \times 10^{-12}$	$7.4 \times 10^2$	$8.5 \times 10^{-13}$	$1.7 \times 10^{-12}$	$4.9 \times 10^{-1}$
Combined	$8.0 \times 10^{-10}$	$1.3 \times 10^{-13}$	$6.2 \times 10^3$	$9.5 \times 10^{-14}$	$1.5 \times 10^{-13}$	$6.3 \times 10^{-1}$

TABLE IV. Same as Table III but with realistic masks, i.e., the resolvable CBC events are injected using the recovered parameters.

found after notching to be flat. This simple assumption is good enough to demonstrate that the masking procedure is efficient at removing the astrophysical foreground.

By comparing Tables III and IV, we notice that the

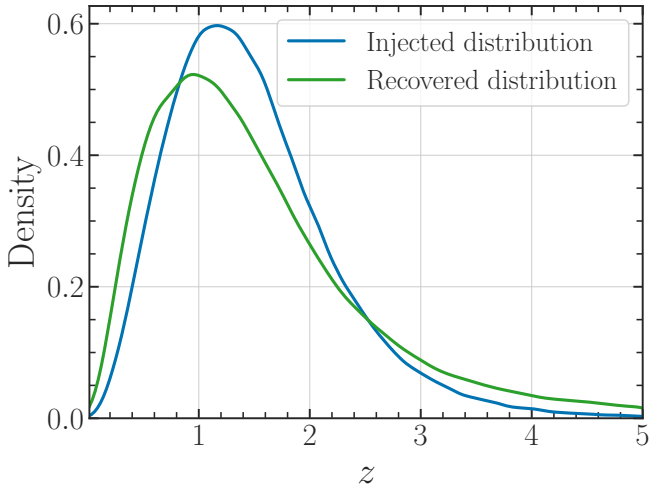


FIG. 6. The injected (blue) and recovered (green) redshift distribution up to  $z = 5$ .

injection of resolvable CBC events with recovered parameters leads to a much louder foreground: before notching we have  $\hat{C} = 3.0 \times 10^{-10}$  combined among all baselines for the injection with true parameters (Table III), and  $\hat{C} = 8.0 \times 10^{-10}$  for the injection with recovered parameters (Table IV).

We explain why this is the case in Fig. 6, where we compare the injected and recovered redshift distributions for the resolved CBC signals. We show the distribution only up to  $z = 5$  because the main contribution to the astrophysical stochastic foreground comes from this redshift range [67]. By drawing resampled parameters according to the Fisher errors, the resulting redshift distribution broadens, leading to a less peaked profile. Consequently, the recovered CBC event catalog includes a larger number of nearby events compared to the original injected catalog, resulting in a louder astrophysical foreground.

- [1] R. Abbott et al. (KAGRA, VIRGO, LIGO Scientific), *Phys. Rev. X* **13**, 011048 (2023), arXiv:2111.03634 [astro-ph.HE].
- [2] R. Abbott et al. (KAGRA, Virgo, LIGO Scientific), *Phys. Rev. D* **104**, 022004 (2021), arXiv:2101.12130 [gr-qc].
- [3] A. I. Renzini, B. Goncharov, A. C. Jenkins, and P. M. Meyers, *Galaxies* **10**, 34 (2022), arXiv:2202.00178 [gr-qc].
- [4] V. Ferrari, S. Matarrese, and R. Schneider, *Mon. Not. Roy. Astron. Soc.* **303**, 247 (1999), arXiv:astro-ph/9804259.
- [5] A. Buonanno, G. Sigl, G. G. Raffelt, H.-T. Janka, and E. Muller, *Phys. Rev. D* **72**, 084001 (2005), arXiv:astro-ph/0412277.
- [6] K. Crocker, V. Mandic, T. Regimbau, K. Belczynski, W. Gladysz, K. Olive, T. Prestegard, and E. Vangioni, *Phys. Rev. D* **92**, 063005 (2015), arXiv:1506.02631 [gr-qc].
- [7] K. Crocker, T. Prestegard, V. Mandic, T. Regimbau, K. Olive, and E. Vangioni, *Phys. Rev. D* **95**, 063015 (2017), arXiv:1701.02638 [astro-ph.CO].
- [8] B. Finkel, H. Andresen, and V. Mandic, *Phys. Rev. D* **105**, 063022 (2022), arXiv:2110.01478 [gr-qc].
- [9] L. P. Grishchuk, *Zh. Eksp. Teor. Fiz.* **67**, 825 (1974).
- [10] A. A. Starobinsky, *JETP Lett.* **30**, 682 (1979).
- [11] L. P. Grishchuk, *Phys. Rev. D* **48**, 3513 (1993), arXiv:gr-qc/9304018.
- [12] N. Barnaby, E. Pajer, and M. Peloso, *Phys. Rev. D* **85**, 023525 (2012), arXiv:1110.3327 [astro-ph.CO].
- [13] T. Damour and A. Vilenkin, *Phys. Rev. D* **71**, 063510 (2005), arXiv:hep-th/0410222.
- [14] X. Siemens, V. Mandic, and J. Creighton, *Phys. Rev. Lett.* **98**, 111101 (2007), arXiv:astro-ph/0610920.
- [15] S. Olmez, V. Mandic, and X. Siemens, *Phys. Rev. D* **81**, 104028 (2010), arXiv:1004.0890 [astro-ph.CO].
- [16] T. Regimbau, S. Giampanis, X. Siemens, and V. Mandic, *Phys. Rev. D* **85**, 066001 (2012), arXiv:1111.6638 [astro-ph.CO].
- [17] R. Abbott et al. (LIGO Scientific, Virgo), *Astrophys. J. Lett.* **913**, L7 (2021), arXiv:2010.14533 [astro-ph.HE].
- [18] S. S. Bavera, G. Franciolini, G. Cusin, A. Riotto, M. Zevin, and T. Fragos, *Astron. Astrophys.* **660**, A26 (2022), arXiv:2109.05836 [astro-ph.CO].
- [19] D. Reitze, R. X. Adhikari, S. Ballmer, B. Barish, L. Barsotti, G. Billingsley, D. A. Brown, Y. Chen, D. Coyne, R. Eisenstein, et al., arXiv:1907.04833 (2019).
- [20] M. Punturo, M. Abernathy, F. Acernese, et al., *Classical and Quantum Gravity* **27**, 194002 (2010).
- [21] M. Evans, R. X. Adhikari, C. Afle, et al., “A horizon study for cosmic explorer: Science, observatories, and community,” (2021).
- [22] M. Branchesi et al., *JCAP* **07**, 068 (2023), arXiv:2303.15923 [gr-qc].
- [23] T. Regimbau, M. Evans, N. Christensen, E. Katsavounidis, B. Sathyaprakash, and S. Vitale, *Phys. Rev. Lett.* **118**, 151105 (2017), arXiv:1611.08943 [astro-ph.CO].
- [24] S. Sachdev, T. Regimbau, and B. S. Sathyaprakash, *Phys. Rev. D* **102**, 024051 (2020), arXiv:2002.05365 [gr-qc].
- [25] B. Zhou, L. Reali, E. Berti, M. Çalıřkan, C. Creque-Sarbinowski, M. Kamionkowski, and B. S. Sathyaprakash, *Phys. Rev. D* **108**, 064040 (2023), arXiv:2209.01310 [gr-qc].
- [26] B. Zhou, L. Reali, E. Berti, M. Çalıřkan, C. Creque-Sarbinowski, M. Kamionkowski, and B. S. Sathyaprakash, arXiv (2022), arXiv:2209.01221 [gr-qc].
- [27] H. Song, D. Liang, Z. Wang, and L. Shao, *Phys. Rev. D* **109**, 123014 (2024), arXiv:2401.00984 [gr-qc].
- [28] C. Cutler and J. Harms, *Phys. Rev. D* **73**, 042001 (2006), arXiv:gr-qc/0511092.
- [29] A. Sharma and J. Harms, *Phys. Rev. D* **102**, 063009 (2020), arXiv:2006.16116 [gr-qc].
- [30] Z. Pan and H. Yang, *Phys. Rev. D* **107**, 123036 (2023), arXiv:2301.04529 [gr-qc].
- [31] M. Li, J. Yu, and Z. Pan, arXiv (2024), arXiv:2403.01846 [gr-qc].
- [32] R. Smith and E. Thrane, *Phys. Rev. X* **8**, 021019 (2018), arXiv:1712.00688 [gr-qc].
- [33] R. J. E. Smith, C. Talbot, F. Hernandez Vivanco, and E. Thrane, *Mon. Not. Roy. Astron. Soc.* **496**, 3281 (2020), arXiv:2004.09700 [astro-ph.HE].
- [34] S. Biscoveanu, C. Talbot, E. Thrane, and R. Smith, *Phys. Rev. Lett.* **125**, 241101 (2020), arXiv:2009.04418 [astro-ph.HE].
- [35] H. Zhong, R. Ormiston, and V. Mandic, *Phys. Rev. D* **107**, 064048 (2023), [Erratum: *Phys.Rev.D* 108, 089902 (2023)], arXiv:2209.11877 [gr-qc].
- [36] L. S. Finn, *Phys. Rev. D* **46**, 5236 (1992), arXiv:gr-qc/9209010.
- [37] N. Aghanim et al. (Planck), *Astron. Astrophys.* **641**, A6 (2020), [Erratum: *Astron.Astrophys.* 652, C4 (2021)], arXiv:1807.06209 [astro-ph.CO].
- [38] B. Allen and J. D. Romano, *Phys. Rev. D* **59**, 102001 (1999), arXiv:gr-qc/9710117.
- [39] P. Landry and J. S. Read, *Astrophys. J. Lett.* **921**, L25 (2021), arXiv:2107.04559 [astro-ph.HE].
- [40] G. M. Harry (LIGO Scientific), *Class. Quant. Grav.* **27**, 084006 (2010).
- [41] J. Aasi et al. (LIGO Scientific), *Class. Quant. Grav.* **32**, 074001 (2015), arXiv:1411.4547 [gr-qc].
- [42] F. Acernese et al. (VIRGO), *Class. Quant. Grav.* **32**, 024001 (2015), arXiv:1408.3978 [gr-qc].
- [43] V. Srivastava, D. Davis, K. Kuns, P. Landry, S. Ballmer, M. Evans, E. D. Hall, J. Read, and B. S. Sathyaprakash, *Astrophys. J.* **931**, 22 (2022), arXiv:2201.10668 [gr-qc].
- [44] G. Pratten, S. Husa, C. Garcia-Quiros, M. Colleoni, A. Ramos-Buades, H. Estelles, and R. Jaume, *Phys. Rev. D* **102**, 064001 (2020), arXiv:2001.11412 [gr-qc].
- [45] M. Vallisneri, *Phys. Rev. D* **77**, 042001 (2008), arXiv:gr-qc/0703086.
- [46] S. Borhanian, *Class. Quant. Grav.* **38**, 175014 (2021), arXiv:2010.15202 [gr-qc].
- [47] S. Wu and A. H. Nitz, *Phys. Rev. D* **107**, 063022 (2023), arXiv:2209.03135 [astro-ph.IM].
- [48] L. Reali, A. Antonelli, R. Cotesta, S. Borhanian, M. Çalıřkan, E. Berti, and B. S. Sathyaprakash, (2022), arXiv:2209.13452 [gr-qc].
- [49] L. Reali, A. Maselli, and E. Berti, (2023), arXiv:2307.01264 [gr-qc].
- [50] A. D. Johnson, K. Chatziioannou, and W. M. Farr, arXiv (2024), arXiv:2402.06836 [gr-qc].
- [51] Y. Himemoto, A. Nishizawa, and A. Taruya, *Phys. Rev. D* **104**, 044010 (2021), arXiv:2103.14816 [gr-qc].

- [52] E. Pizzati, S. Sachdev, A. Gupta, and B. Sathyaprakash, *Phys. Rev. D* **105**, 104016 (2022), [arXiv:2102.07692 \[gr-qc\]](#).
- [53] A. Samajdar, J. Janquart, C. Van Den Broeck, and T. Dietrich, *Phys. Rev. D* **104**, 044003 (2021), [arXiv:2102.07544 \[gr-qc\]](#).
- [54] J. Janquart, T. Baka, A. Samajdar, T. Dietrich, and C. Van Den Broeck, (2022), [arXiv:2211.01304 \[gr-qc\]](#).
- [55] D. Meacher, M. Coughlin, S. Morris, T. Regimbau, N. Christensen, S. Kandhasamy, V. Mandic, J. D. Romano, and E. Thrane, *Phys. Rev. D* **92**, 063002 (2015), [arXiv:1506.06744 \[astro-ph.HE\]](#).
- [56] T. Regimbau et al., “MDC\_Generation,” .
- [57] G. Ashton et al., *Astrophys. J. Suppl.* **241**, 27 (2019), [arXiv:1811.02042 \[astro-ph.IM\]](#).
- [58] S. Sachdev et al., *Astrophys. J. Lett.* **905**, L25 (2020), [arXiv:2008.04288 \[astro-ph.HE\]](#).
- [59] A. I. Renzini et al., *Astrophys. J.* **952**, 25 (2023), [arXiv:2303.15696 \[gr-qc\]](#).
- [60] P. C. Peters and J. Mathews, *Phys. Rev.* **131**, 435 (1963).
- [61] S. Borhanian and B. S. Sathyaprakash, (2022), [arXiv:2202.11048 \[gr-qc\]](#).
- [62] F. Iacovelli, M. Mancarella, S. Foffa, and M. Maggiore, *Astrophys. J.* **941**, 208 (2022), [arXiv:2207.02771 \[gr-qc\]](#).
- [63] M. Pieroni, A. Ricciardone, and E. Barausse, *Sci. Rep.* **12**, 17940 (2022), [arXiv:2203.12586 \[astro-ph.CO\]](#).
- [64] A. Boesky, F. S. Broekgaarden, and E. Berger, (2024), [arXiv:2405.01630 \[astro-ph.HE\]](#).
- [65] A. Boesky, F. S. Broekgaarden, and E. Berger, (2024), [arXiv:2405.01623 \[astro-ph.HE\]](#).
- [66] D. S. Bellie, S. Banagiri, Z. Doctor, and V. Kalogera, (2023), [arXiv:2310.02517 \[gr-qc\]](#).
- [67] A. I. Renzini, T. A. Callister, K. Chatziioannou, and W. M. Farr, (2024), [arXiv:2403.14793 \[astro-ph.HE\]](#).
- [68] M. Pieroni and E. Barausse, *JCAP* **07**, 021 (2020), [Erratum: *JCAP* 09, E01 (2020)], [arXiv:2004.01135 \[astro-ph.CO\]](#).
- [69] J. Alvey, U. Bhardwaj, V. Domcke, M. Pieroni, and C. Weniger, *Phys. Rev. D* **109**, 083008 (2024), [arXiv:2309.07954 \[gr-qc\]](#).
- [70] D. Stanzione, J. West, R. T. Evans, T. Minyard, O. Ghattas, and D. K. Panda, in [Practice and Experience in Advanced Research Computing](#), PEARC '20 (Association for Computing Machinery, New York, NY, USA, 2020) p. 106–111.
- [71] A. J. Farmer and E. S. Phinney, *Mon. Not. Roy. Astron. Soc.* **346**, 1197 (2003), [arXiv:astro-ph/0304393](#).